Research Article Vol. 40, No. 12 / December 2023 / Journal of the Optical Society of America A 2177

Journal of the Optical Society of America A
OPTICS, IMAGE SCIENCE, AND VISION

Surface plasmon resonance sensor composed of micro-nano optical fibers for high-sensitivity refractive index detection

Haihao Fu,[1] Chao Liu,[1,*] Luhui Xu,[1] Wei Liu,[1] Jingwei Lv,[1] Jianxin Wang,[1] Jie He,[1] Xingdi Luo,[1] and Paul K. Chu[2,3,4]

[1]School of Physics and Electronic Engineering, Northeast Petroleum University, Daqing 163318, China
[2]Department of Physics, City University of Hong Kong, Tat Chee Avenue, Kowloon, Hong Kong, China
[3]Department of Materials Science and Engineering, City University of Hong Kong, Tat Chee Avenue, Kowloon, Hong Kong, China
[4]Department of Biomedical Engineering, City University of Hong Kong, Tat Chee Avenue, Kowloon, Hong Kong, China
*msm-liu@126.com

Received 6 July 2023; revised 11 October 2023; accepted 26 October 2023; posted 27 October 2023; published 15 November 2023

Spurred by the continuous development of surface plasmon resonance (SPR) technology, optical fiber sensors based on SPR have become a research hotspot. Although single-mode fibers (SMFs) are simple and easy to manufacture, the sensitivity is quite poor. On the other hand, even though photonic crystal fibers (PCFs) and anti-resonant fibers (ARFs) can achieve high-sensitivity detection and the wavelength sensitivity is tens of times that of SMFs, they are complex and difficult to produce. Herein, an SPR refractive index sensor composed of micro-nano optical fibers (MNFs) is designed to detect analytes in the refractive index range between 1.33 and 1.43. Analysis by the finite element method (FEM) reveals that the maximum wavelength sensitivity is 49,000 nm/RIU. The SPR sensor boasting a simple structure, low cost, and high wavelength sensitivity has enormous potential in applications such as chemical analysis, environmental monitoring, and other fields.

https://doi.org/10.1364/JOSAA.499894

1. INTRODUCTION

Optical fiber sensors are frequently used to monitor variations in temperature, gas concentration, refractive index, and other physical entities by modulating the amplitude, polarization, frequency, and phase of the incident light [1,2]. They have attracted widespread interest due to their excellent electrical insulation, strong resistance to electromagnetic interference, and high sensitivity [3]. Common optical fiber sensors include the F-P air bubble microcavity sensors [4], fiber grating sensors [5], and surface plasmon resonance (SPR) fiber sensors [6–8]. However, F-P air bubble microcavity sensors can only measure microstrain, while fiber grating sensors are not suitable for dynamic signal measurements. On the other hand, SPR sensors have attracted attention in optical fiber sensing because of their ability to detect a number of entities including the temperature, magnetic field strength, gas concentration, and liquid refractive index in real-time. SPR is an optical phenomenon in which when light with a certain frequency impinges the dielectric surface of two media with different refractive indexes, the evanescent waves produced propagate along the dielectric surface [9]. Coupling of the surface plasmon wave (SPW) [10] on the surface of metal materials with the evanescent waves causes a portion of the energy of incident light to be transferred to the surface plasmon, and the frequency of energy transfer for different refractive indexes exhibits regularity thus enabling fiber sensing.

Several types of optical fibers can be used for SPR sensing, for example, the single-mode fiber (SMF) [11], photonic crystal fiber (PCF) [12–18], and anti-resonant fiber (ARF) [19,20]. Slavík *et al*. [21] have designed an SMF-SPR sensor for liquid detection in the refractive index range of 1.3302–1.3422 with a maximum sensitivity of 3900 nm/RIU. Q.M. Kamrunnahar *et al*. [22] have proposed a circular lattice dual-core PCF-SPR sensor showing a maximum sensitivity of 11,200 nm/RIU, and Lv [23] have analyzed a double resonant peak liquid refractive index ARF-SPR sensor and demonstrated wavelength sensitivities of 20,000 nm/RIU and 36,400 nm/RIU. Nevertheless, SMF-SPRs have low sensitivity. Although the sensitivity of PCF-SPR and ARF-SPR sensors is better, the manufacturing process is complex and expensive.

The micro-nano fiber (MNF) [24], a waveguide with a diameter close to that of the transmission wavelength, can be prepared by physically stretching the SMF. It has the advantages of low cost, good uniformity, and easy mass production. In addition, the small surface roughness of MNFs enables low-loss transmission of evanescent waves to not only improve the near-field optical coupling between the MNF and other structures, but also enhance the sensitivity of the MNF sensor. When the

MNF is utilized as the medium in the SPR sensor, the sensitivity is improved significantly while the production difficulty can be reduced.

Herein, an SPR refractive index sensor consisting of three MNFs stacked and embedded with a gold wire is designed and analyzed by the finite element method using the COMSOL software. The mode coupling, wavelength sensitivity, FOM, and other parameters are analyzed. Our results disclose that the MNF-SPR sensor can detect liquid refractive indexes in the range of 1.33–1.43 with average wavelength sensitivity and minimum structural parameter sensitivity of 27,454.55 nm/RIU and 50 nm/μm, respectively, in addition to good stability. The sensor has large commercial potential in many fields such as petroleum, logging, chemical analysis, and biomedical engineering.

Additionally, the main objectives of the research are listed as follows:

1. analyzing the basic principle of SPR refractive index sensors;
2. designing a kind of refractive index sensor composed of three MNFs based on SPR, and obtaining the best performance parameters through detailed structural optimization;
3. calculating and analyzing the characteristic of mode coupling, refractive index sensing, structural parameter sensitivity, FOM and SNR, detection distance, and sensing length with FEM.

2. BASIC THEORY AND MNF DESIGN

When light with a certain frequency impinges on a metal surface, the uniform distribution of electron density is broken. The positively charged particles in the region cannot be completely neutralized when the regional electron density is less than the average electron density, resulting in positive electricity. To restore electrical neutrality, electrons are attracted to the region. The kinetic energy of electrons is greater than repulsion resulting in electron aggregation. If there are enough electrons, the repulsive force between them will be greater than the attraction by the positive charge, consequently driving the electrons away. When electrons undergo cyclic motion on the metal surface, free electrons and photons on the surface will interact with each other at the dielectric interface to generate electromagnetic modes. After being excited by an external electromagnetic field, free electrons undergo quantum oscillations in the background of positive ions, producing SPP [25]. The energy field generated is called the SPW, and the propagation constant of SPW is shown in Eq. (1) [26]:

$$K_{\mathrm{spw}} = \frac{\omega}{c}\sqrt{\frac{\varepsilon_m(\omega)\varepsilon_2}{\varepsilon_m(\omega)+\varepsilon_2}}, \tag{1}$$

where $\varepsilon_m(\omega)$ and ε_2 are the dielectric constants of the metal and optically sparse medium, respectively, and ω is the frequency of the incident light wave. In addition, when the beam passes from a light-dense medium to a light-sparse medium, it does not immediately reflect on the medium surface. Instead, it first penetrates the light-sparse medium at a depth of about one wavelength, and then drifts along the surface for about half a wavelength before returning to the light-dense medium. The wave propagating along the interface between two media is the evanescent wave, and the propagation constant can be obtained by Eq. (2) [27]:

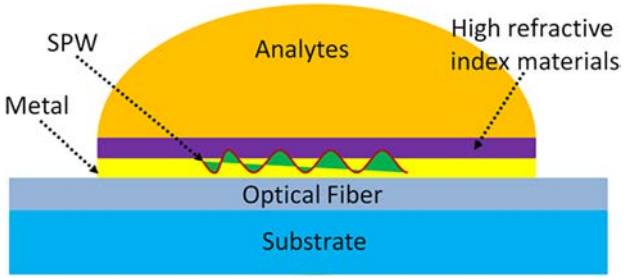

Fig. 1. Basic principles of SPR.

$$K = \frac{\omega}{c}\sqrt{\varepsilon_1(\omega)}\sin\theta_i, \tag{2}$$

where ω is the frequency of the incident light, ε_1 is the dielectric constant of the optically dense medium at this frequency, c is the speed of light, and θ_i is the incident angle of the light wave. When the propagation constant of SPW and the evanescent wave is consistent, SPR is excited and the intensity of the reflected light decreases. Figure 1 shows the schematic diagram of SPR excitation.

Owing to the strong evanescent field characteristics of MNF, coupling with SPW is enhanced, boding well for refractive index detection. As for the MNF-SPR sensor, the MNF and analytes are light-dense medium and light-sparse medium, respectively. SPR involves the energy exchange between the guided mode and SPP mode, which can be characterized by the confinement loss shown in Eq. (3) [28]:

$$L = \frac{2\pi}{\lambda}\frac{20}{\ln(10)}10^4\,\mathrm{Im}(n_{\mathrm{eff}})/(\mathrm{dB/cm}), \tag{3}$$

where λ is the wavelength, and $\mathrm{Im}(n_{\mathrm{eff}})$ is the imaginary part of the effective refractive index. As the wavelength red-shifts, electrons gather gradually, and the energy increases. Electrons then disperse gradually because of repulsion, resulting in a loss trend that increases initially and then decreases. The reflected light intensity is the lowest when the loss reaches the maximum, which reflects the mode coupling. The corresponding wavelength is defined as the resonance wavelength. By inspecting the loss spectrum of the analyte, the refractive index can be derived because different optical sparse media produce different loss curves and resonance wavelengths. Here, in order to accomplish high-sensitivity refractive index detection, the fiber structure depicted in Fig. 2 is designed.

The SPR sensor consists of three MNFs with a refractive index difference of 1.5% arranged in a triangular structure. A gold wire with a diameter of d_a is inlaid in the center, and the relative dielectric constant is determined by Eq. (4) [29]:

$$\varepsilon_{\mathrm{Au}}(\omega) = \varepsilon_\infty - \frac{\omega_p^2}{\omega(\omega + i\omega_\tau)}, \tag{4}$$

where $\varepsilon_\infty = 9.75$, $\omega_p = 1.36\times10^{16}$ rad/s, and $\omega_\tau = 1.45\times10^{14}$ rad/s, and the gold wire is tangent to the three

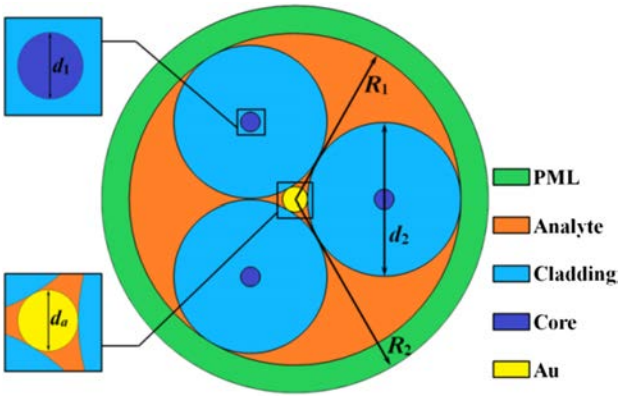

Fig. 2. Cross-section of the MNF-SPR sensor.

MNFs. The preparation is simplified compared to traditional coating methods when inlaying the gold wire. The light blue area is the cladding of the MNF with a diameter of d_2 and made of SiO_2 of which the refractive index is determined by the Sellmeier equation [30]

$$n^2(\lambda) = 1 + \frac{A_1\lambda^2}{\lambda^2 - B_1} + \frac{A_2\lambda^2}{\lambda^2 - B_2} + \frac{A_3\lambda^2}{\lambda^2 - B_3}, \tag{5}$$

where $A_1 = 0.6961663$, $A_2 = 0.4079426$, $A_3 = 0.897479$, $B_1 = 0.0684043$, $B_2 = 0.1162414$, and $B_3 = 9.896161$. The dark blue area is the core with a diameter of d_1, and the corresponding refractive index is determined by Eq. (6) [31]:

$$\Delta = \frac{n_1^2 - n_2^2}{2n_1^2}, \tag{6}$$

where $\Delta = 1.5\%$ is the relative refractive index difference, and n_1 and n_2 are the refractive indexes of the core and cladding, respectively. The orange area is the analyte, and the MNF-SPR sensor can be placed directly in the liquid for refractive index detection without filling, consequently simplifying the detection process compared to many structures [32–34]. The green area is the perfect matching layer (PML), which absorbs all the electromagnetic radiation and provides the perfect boundary conditions for the simulation.

Wavelength sensitivity is the most important measure of whether refractive index sensors have practical application value. On the one hand, wavelength sensitivity determines the accuracy of the sensor; on the other hand, with the change of fiber structure parameters, the change in wavelength sensitivity is more significant compared to other performance. Therefore, choosing wavelength sensitivity as the standard for performance optimization is more reasonable. The wavelength sensitivity is defined as the ratio of the resonance wavelength difference to the refractive index difference of adjacent analytes, as shown in Eq. (7) [35]:

$$S_n = \frac{\Delta\lambda_{\text{peak}}}{\Delta n_a}, \tag{7}$$

where $\Delta\lambda_{\text{peak}}$ and Δn_a are the variations of the resonance wavelength and refractive index of the analyte, respectively. In order to improve the characteristics of the MNF-SPR refractive index sensor, the diameters of the fiber core, gold wire, and cladding

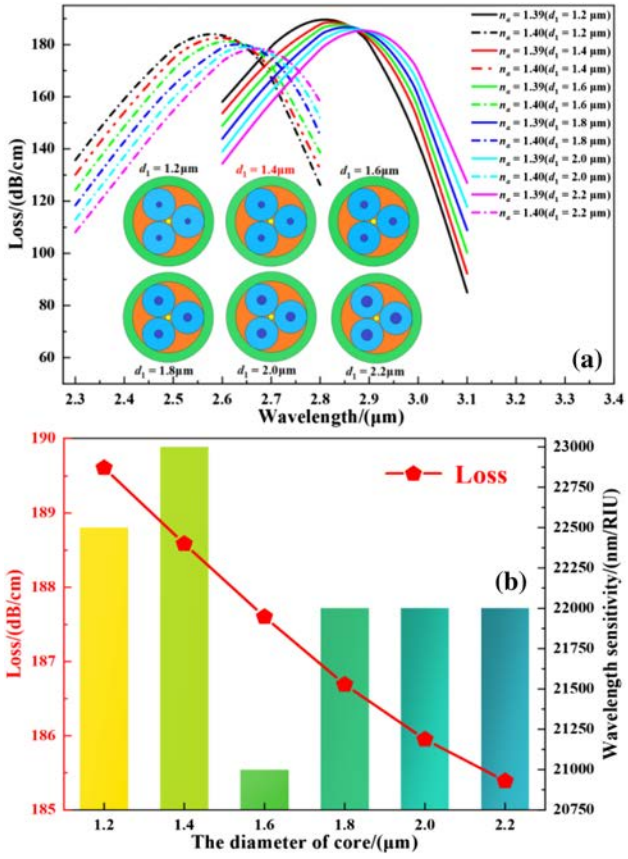

Fig. 3. (a) Loss curves for different core diameters and (b) wavelength sensitivity when the refractive index of the analyte is 1.39.

are systematically optimized based on the wavelength sensitivity and confinement loss for an analyte refractive index of 1.39. The basic principle of SPR sensing is the energy coupling between the guided and SPP modes. The former is located in the core, and the latter is mainly excited on the surface of the gold wire. Therefore, it is necessary to first determine the diameter of the core and gold wire. Then, the coupling characteristic between the two modes is decided by the distance between the core and gold wire. Consequently, the fiber optic structure will be optimized in the order of core diameter, wire diameter, and cladding diameter. The initial structural parameters are: $d_1 = 1.6$ μm, $d_a = 1.2$ μm, and $d_2 = 7.0$ μm, and the optimization process is described in the following.

The core diameter is first optimized as shown in Figs. 3(a) and 3(b). When $d_1 < 1.2$ μm, the distance between the core and edge of the cladding is large leading to insufficient evanescent field strength; when $d_1 > 2.2$ μm, the fundamental mode is distorted, and so the range of the core diameter is set to be $1.2\ \mu\text{m} < d_1 < 2.2\ \mu\text{m}$. Figures 2(a) and 2(b) indicate that although the loss at the resonance wavelength is inversely proportional to the core diameter, the change is not significant. In addition, there is no obvious linear relationship between the wavelength sensitivity and d_1 when $n_a = 1.39$. The wavelength sensitivity is the highest (23,000 nm/RIU) when d_1 is 1.4 μm, and therefore, the diameter of the core is set to be 1.4 μm.

The diameter of the gold wire is then adjusted for $d_1 = 1.4$ μm, as shown in Figs. 4(a) and 4(b). The d_a value

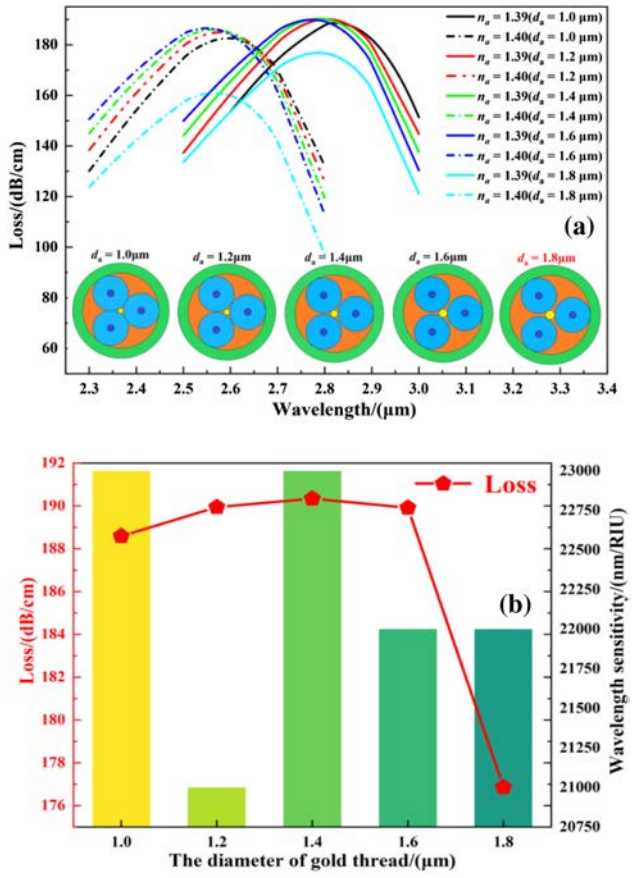

Fig. 4. (a) Loss spectra of the analytes for different d_a and (b) losses at different resonance wavelengths and corresponding sensitivities.

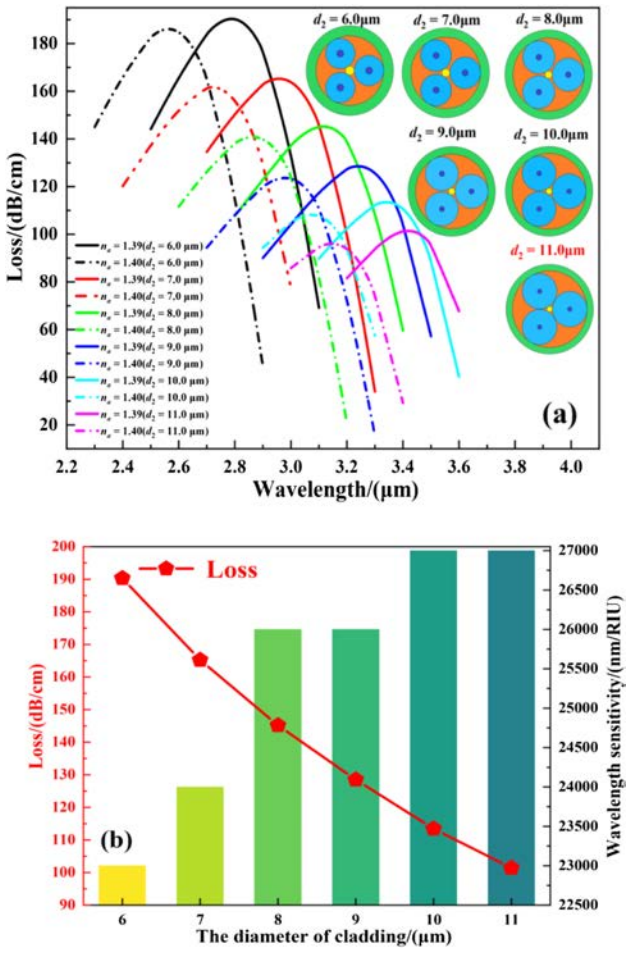

Fig. 5. (a) Loss spectra for different d_2 and (b) wavelength sensitivity when n_a is 1.39.

is optimized within the range of 1.0 μm < d_a < 1.8 μm because if the diameter of the gold wire is less than 1.0 μm, the three MNFs will intersect. When d_a is greater than 1.8 μm, the coupling characteristics between the guided mode and SPP mode are poor. As the size of the gold wire increases, there is no significant change in the wavelength sensitivity and loss. The highest sensitivity is observed when the diameters are 1.0 and 1.4 μm. When $d_a = 1.8$ μm, the loss of the fundamental mode decreases significantly boding well for long-distance detection. Hence, the optimal d_a is 1.8 μm.

After determining the diameters of the core and gold wire, that of the cladding is optimized as shown in Figs. 5(a) and 5(b). When the cladding diameter is less than 6.0 μm, the energy of the core leaks easily into the analyte, resulting in lower sensitivity, but if d_2 is larger than 11.0 μm, the three claddings intersect. Therefore, the cladding diameter is optimized in the range between 6.0 and 11.0 μm. Figures 5(a) and 5(b) show that not only the resonance wavelength red-shifts, but also the loss diminishes significantly when d_2 increases. The reason for this phenomenon is that as the diameter of the cladding increases, the distance between the core of MNF and the gold wire becomes longer, reducing the coupling strength between the core and SPP mode, resulting in lower loss. The wavelength sensitivity is directly proportional to the cladding diameter. When $d_2 = 11$ μm, the loss and wavelength sensitivity exhibit the minimum and maximum values of 101.41 dB/cm and 27,000 nm/RIU, respectively. In summary, the refractive index detection characteristics of the MNF-SPR sensor are the best when $d_1 = 1.4$ μm, $d_a = 1.8$ μm, $d_2 = 11.0$ μm, $R_1 = 23.8$ μm, and $R_2 = 25.8$ μm.

The MNF-SPR sensor can be produced by electrospinning [36] as shown in Fig. 6. The direct-write electrospinning platform includes a high-voltage DC power supply, solution storage device, solution injection mechanism, and fiber collection system. During manufacturing, the solution is poured into a transparent plastic tube between the syringe and needle for backup. The DC high-voltage power supply anode is connected to the syringe and the ground wire to the collector. The voltage and velocity of the fluid are set to predetermined values to control the X–Y motion platform to move along the predetermined path and collect the MNF. In addition, the designed MNF can also be prepared using cone pulling technology. Fix the two ends of a certain size SMF on the pulling cone platform, align the spray gun with the SMF, ignite and heat it, and utilize the computer program to control the stepper motors at both ends of the SMF to evenly rotate and stretch the optical fiber to obtain the proposed MNF. Finally, scanning electron microscopy is performed. The three MNFs are fixed in the triangular structure, and a tungsten wire is used to push the gold wire into the center gap before packaging.

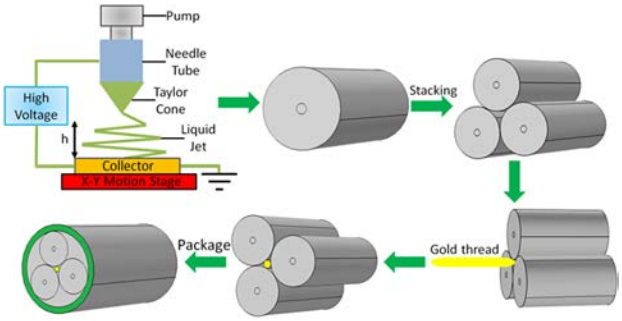

Fig. 6. Preparation of the MNF-SPR sensor by electrospinning and direct writing.

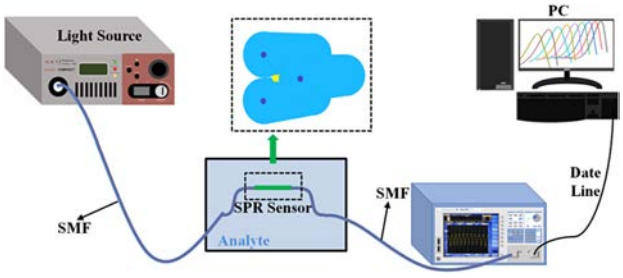

Fig. 7. Schematic showing the detection process by the MNF-SPR sensor.

Figure 7 illustrates the liquid refractive index detection process by the MNF-SPR sensor. Firstly, two SMFs are fused on both sides of the sensor and connected to the light source and optical spectrum analyzer (OSA) connected to a PC. The SPR sensor is placed in the liquid analyte, and after turning on the light, the OSA is adjusted to the appropriate wavelength to calculate the refractive index with the extracted resonance wavelength.

3. RESULTS AND DISCUSSION

The finite element method (FEM) is utilized to determine the mode coupling, wavelength sensitivity, resolution, structural parameter sensitivity, figure of merit (FOM), signal-to-noise ratio (SNR), and sensor length (SL).

A. Coupling Properties

SPR involves the energy exchange between the fundamental mode and SPP mode, the so-called mode coupling that is reflected by the light field distributions of the two modes before and after resonance. Figures 8(a)–8(f) describe the optical field distributions of the fundamental and SPP modes at wavelengths of 3.32 μm, 3.66 μm, and 3.90 μm, respectively, when the refractive index of the analyte is 1.38. Before reaching the resonance wavelength, the electron energy is mainly concentrated in the three cores, while the surface energy of the gold wire is comparatively low. When the wavelength red-shifts to the resonance wavelength, the guided mode energy is gradually transferred to the surface of the gold wire. The core field strength weakens and at the same time, the energy of the SPP mode goes up.

The mode coupling is studied by varying the dispersion of the basic and SPP modes, and the relationship between the loss and

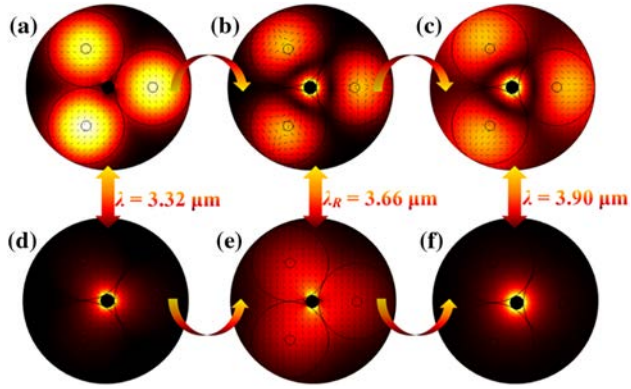

Fig. 8. (a)–(c) Fundamental mode and (d)–(f) SPP mode at wavelengths of 3.32 μm, 3.66 μm, and 3.90 μm when $n_a = 1.38$.

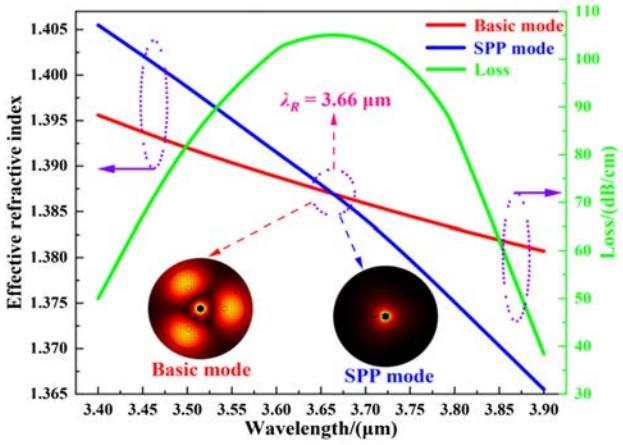

Fig. 9. Relationship between the refractive indexes of the basic and SPP mode with wavelength together with the loss curve of the fundamental mode.

wavelength is presented in Fig. 9. As the wavelength increases, the effective refractive indexes of the guided and SPP modes are inversely proportional to the wavelength. When λ is less than 3.66 μm, the effective refractive index of the SPP mode is greater than that of the basic mode, whereas the opposite is true when $\lambda > 3.66$ μm. Moreover, as the wavelength red-shifts, the loss increases initially and then decreases. At the resonance wavelength, the strongest resonance occurs.

B. Refractive Index Sensing

When the MNF-SPR sensor is placed in analytes with different refractive indexes, different loss curves are shown on the OSA corresponding to different resonance wavelengths. The wavelength sensitivity expressed in Eq. (7) can be calculated based on the variation of the resonance wavelength with n_a, which is an important indicator to gauge the sensor performance. Figures 10(a)–10(c) display the loss curves, resonance wavelengths, corresponding loss peaks, and wavelength sensitivity of different analytes. The MNF-SPR sensor can detect analytes with refractive indexes between 1.33 and 1.43. The trend of all the loss spectra with wavelength is identical, and the peak loss is inversely proportional to the refractive index of the analyte.

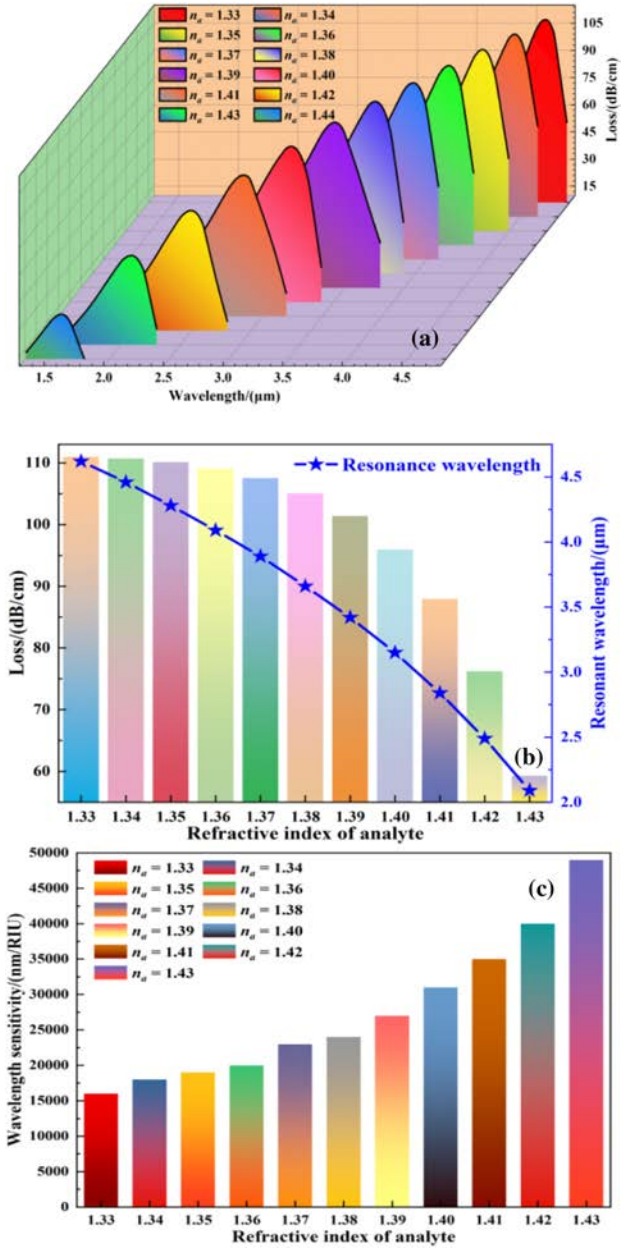

Fig. 10. (a) Loss spectra of different analytes, (b) loss peak and resonance wavelength, and (c) wavelength sensitivity when n_a is 1.33–1.43.

As n_a increases, the resonance wavelength blue-shifts gradually, and the wavelength sensitivity increases significantly. In addition, the sensitivity is above 15,000 nm/RIU, and the wavelength sensitivity shows a maximum value of 49,000 nm/RIU when the refractive index of the analyte is 1.43. The average wavelength sensitivity is 27,454.55 nm/RIU, which is better than that described in Ref. [37].

Linear fitting is performed to obtain the relationship between the refractive index of the analyte and resonance wavelength as shown in Eq. (8):

$$n_a = 1.509 - 0.037\lambda_R, \quad 1.60 \le \lambda_R \le 4.62, \tag{8}$$

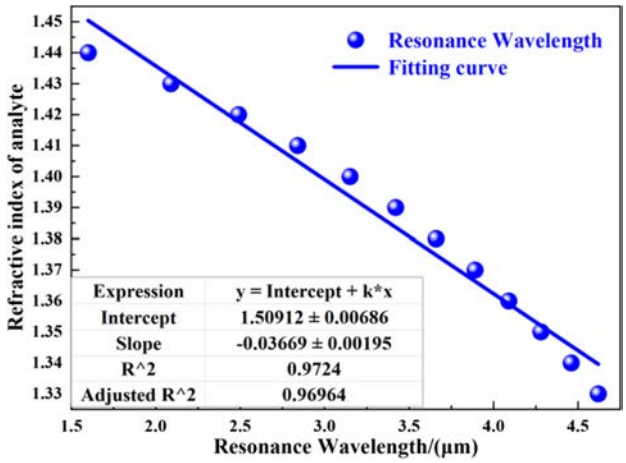

Fig. 11. Linear fitting of the resonance wavelength.

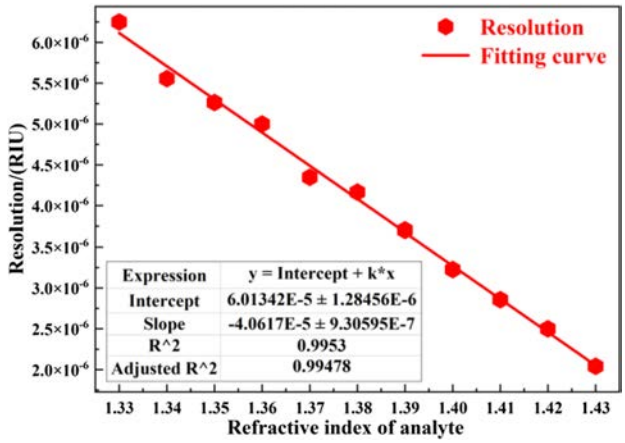

Fig. 12. Linear fitting of the resolution.

where λ_R is the resonance wavelength, n_a is the refractive index of the analyte, and the fitted curve is displayed in Fig. 11. The curve exhibits positive linearity with an adjusted R^2 of 96.96%.

The resolution is an important parameter for SPR sensors as it reflects the ability to detect small changes. The lower the resolution, the higher the accuracy of the sensor. R_n is inversely proportional to the wavelength sensitivity as shown in Eq. (9) [38]:

$$R_n = \frac{\Delta n_a \Delta\lambda_{\min}}{\Delta\lambda_{\text{peak}}} = \frac{\Delta\lambda_{\min}}{S_n}, \tag{9}$$

where S_n is the wavelength sensitivity, and $\Delta\lambda_{\min}$ is the minimum measured value of OSA, which is generally related to the instrument. Under the current conditions, $\Delta\lambda_{\min} = 0.1$ nm. The resolution of the sensor for different n_a is fitted as shown in Fig. 12.

The resolution is inversely proportional to the analyte refractive index and is less than 6.25×10^{-6} RIU. When $n_a = 1.43$, R_n shows the optimal value of 2.04×10^{-6} RIU. The average resolution is 3.64×10^{-6} RIU, and the fitting shows a linearity of 99.48% as shown in Eq. (10):

$$R_n = 6.01 \times 10^{-5} - 4.06 \times 10^{-5} n_a, \quad 1.33 \le n_a \le 1.44, \tag{10}$$

where R_n and n_a are the resolution of the sensor and refractive index of the analyte, respectively.

C. Structural Parameter Sensitivity

Considering the limitations of commercial manufacturing, some differences will exist between the theoretically predicted structural parameters of the MNFs and those of the products. Therefore, it is necessary to evaluate the impact of manufacturing deviations or errors on the fiber size and structural parameters. The structural parameters sensitivity is defined as the ratio of the change in the resonance wavelength for different sizes to the change in the structural parameters. The lower the structural parameters sensitivity, the less is the impact of the MNF size changes on the sensing characteristics. The loss spectra and structural parameter sensitivity with respect to the diameters of the core, gold wire, and cladding for different sizes are displayed in Figs. 13(a)–13(f).

As the diameters of the core and gold wire increase, the resonance wavelength demonstrates a trend of red- and blue-shifts, respectively, and the loss decreases slightly. Although the structural parameter sensitivity exhibits no obvious variation with the diameters of the core and gold wire, the sensitivity for d_1 and d_a is lower than 200 nm/μm and 100 nm/μm, respectively, and the minimum is 50 nm/μm, which is far better than that described in Ref. [39]. When the cladding diameter increases, the resonance wavelength red-shifts and the loss peak and structural parameter sensitivity are inversely proportional to d_2. The optimal sensitivity is 80 nm/μm indicating high tolerance.

In order to further investigate the sensing characteristics of the actual MNFs, linear fitting of the resonance wavelength is performed with d_1, d_a, and d_2 as shown in Figs. 14(a)–14(c). When the sensor is prepared, the actual structural parameters may be different from the expected, which will lead to varying characteristics for sensing. In addition, premeasuring the spectrum of the sensor will significantly increase the cost. If

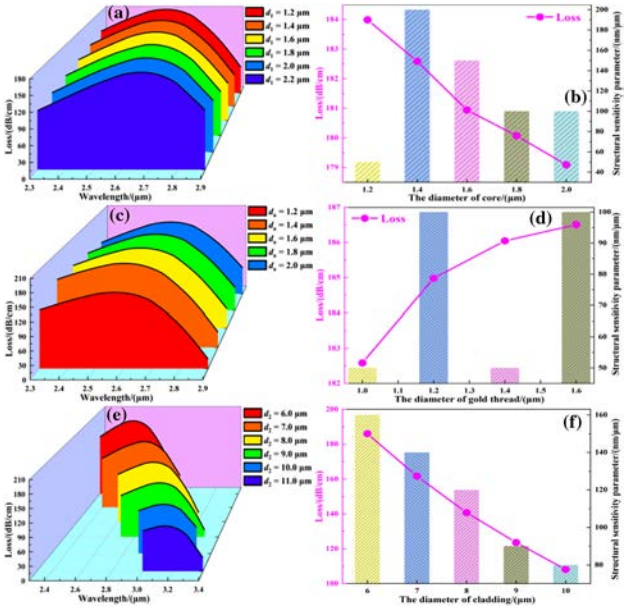

Fig. 13. (a), (c), (e) Loss spectra and (b), (d), (f) structural parameter sensitivity for different d_1, d_a, and d_2 when the refractive index of the analyte is 1.40.

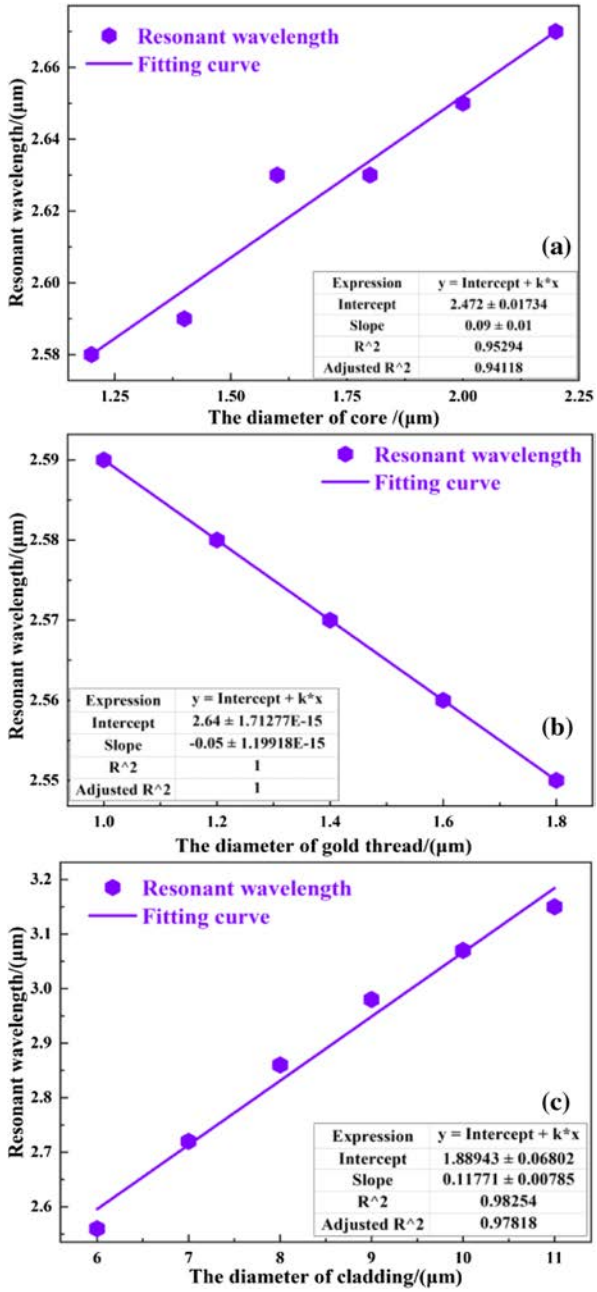

Fig. 14. Linearly fitted curves of the resonance wavelength with the diameters of (a) core, (b) gold wire, and (c) cladding when $n_a = 1.40$.

the relationship between the structural parameters of MNFs and the resonance wavelength can be obtained, the resonance wavelength can be corrected only by measuring the actual size of the fiber. The relationships are shown in Eqs. (11)–(13):

$$\lambda_{R_1} = 2.47 + 0.09d_1, \quad 1.2\ \mu\text{m} \le d_1 \le 2.2\ \mu\text{m}, \tag{11}$$

$$\lambda_{R_2} = 2.64 - 0.05d_a, \quad 1.0\ \mu\text{m} \le d_a \le 1.8\ \mu\text{m}, \tag{12}$$

$$\lambda_{R_3} = 1.89 + 0.12d_2, \quad 6.0\ \mu\text{m} \le d_2 \le 10.0\ \mu\text{m}, \tag{13}$$

where d_1, d_a, and d_2 are the diameters of the core, gold wire, and cladding, respectively. The adjusted R^2 values are 94.12%, 100%, and 97.82% revealing high linearity.

D. FOM and SNR

The figure of merit (FOM) not only represents the degree of energy loss of the output signal of the optical fiber sensor at different frequencies, but is a measure of signal quality that can be used to characterize the overall characteristics of the sensor. The FOM shown in Eq. (14) [40] is an important parameter for refractive index sensors and is defined as the ratio of the wavelength sensitivity to the full-width at half-maximum (FWHM):

$$\mathrm{FOM} = \frac{S_n}{\mathrm{FWHM}}, \tag{14}$$

where S_n is the wavelength sensitivity, and FWHM refers to the frequency band corresponding to half the height of the loss spectrum. The desirable refractive index sensor should have high sensitivity and small FWHM. In addition, as optical fibers are sensitive to the surroundings, the signal-to-noise ratio (SNR) affects the quality of optical signals. The SNR is calculated by Eq. (15) [41]:

$$\mathrm{SNR} = \frac{\Delta\lambda_R}{\mathrm{FWHM}}, \tag{15}$$

where $\Delta\lambda_R$ is the variation of the resonance wavelength. The FOM and SNR of the MNF-SPR sensor are shown in Figs. 15(a) and 15(b). As the refractive index of the analyte increases, both FOM and SNR are proportional to n_a, and the trends are similar. Although there is no noticeable linear relationship between the refractive index and FWHM, it is positively correlated with the difference in the resonance wavelength. When n_a is 1.43, both the FOM and SNR attain the maximum values of 90.404 RIU^{-1} and 0.904, respectively.

E. Detection Distance and Sensor Length

The sensor length (SL) is inversely proportional to the loss at the resonance wavelength as shown by Eq. (16) [42]:

$$\mathrm{SL} = \frac{1}{\alpha(\lambda, n_a)}, \tag{16}$$

where $\alpha(\lambda, n_a)$ is the confinement loss at the resonance wavelength. Figure 16 indicates that as the refractive index increases, the length of the sensor increases gradually. In the n_a range between 1.33 and 1.40, the change in the SL is not appreciable. When $n_a \geq 1.40$, SL increases and the maximum is 288.46 μm.

F. Comparison of Sensing Characteristics

To illustrate the advantages of our MNF-SPR sensor, Table 1 compares the characteristics of representative refractive index sensors reported recently. Our MNF-SPR sensor has significant advantages in terms of the detection range, wavelength sensitivity, resolution, and other properties. In addition, the MNF is very easy to prepare and inexpensive, and embedding a gold wire is simpler than coating it with a gold film.

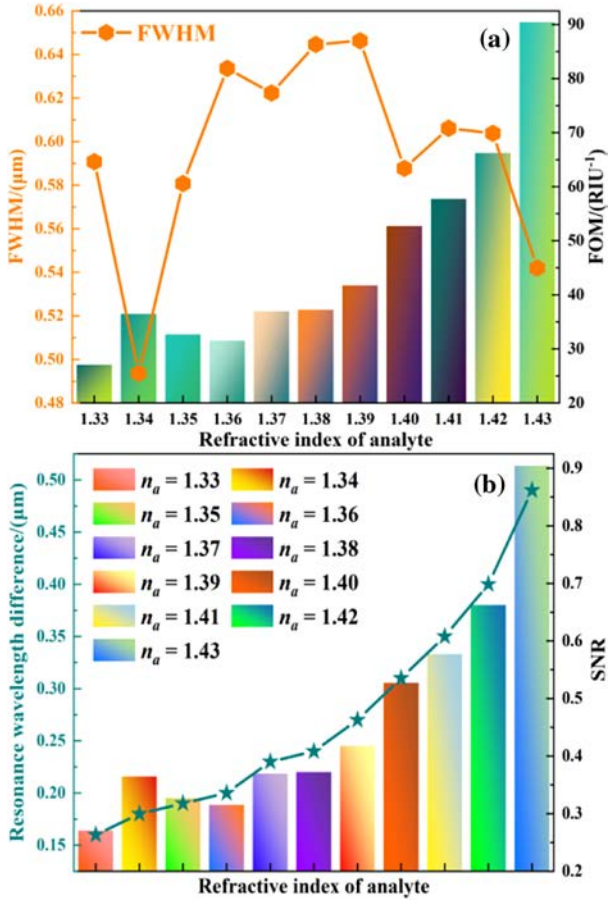

Fig. 15. FOM and SNR of the MNF-SPR sensor.

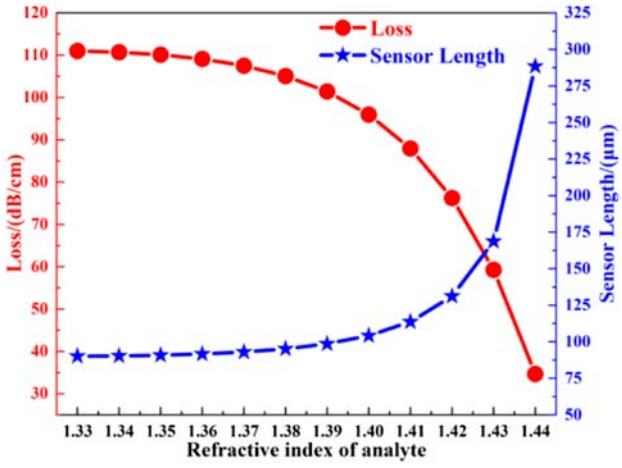

Fig. 16. Relationship between the SL and analyte refractive index.

4. CONCLUSION

An SPR sensor based on MNFs is designed and analyzed by the finite element method. The sensor is composed of three MNFs stacked in a triangular arrangement. A gold wire is embedded in the center for the detection of the refractive indexes of liquid

Table 1. Performance Comparison

Reference	Fiber	Metal	Detection Range	Wavelength Sensitivity	Resolution	Cross-Section
[43]	PCF	TiN	1.385–1.400	10,000 nm/RIU	2.00×10^{-5} RIU	
[38]	PCF	Ag	1.330–1.370	4200 nm/RIU	3.33×10^{-5} RIU	
[37]	PCF	Au	1.330–1.370	4000 nm/RIU	2.50×10^{-5} RIU	
[35]	PCF	Au	1.420–1.460	15,000 nm/RIU	6.67×10^{-6} RIU	
[23]	ARF	Au	1.310–1.445	36,400 nm/RIU	2.75×10^{-6} RIU	
This work	*MNF*	*Au*	*1.330–1.430*	*49,000 nm/RIU*	2.04×10^{-6} RIU	

analytes ranging from 1.33 to 1.43. Systematic optimization of the fiber core diameter, gold wire diameter, and cladding diameter indicates that the optimal structural parameters are: $d_1 = 1.4\ \mu m$, $d_a = 1.8\ \mu m$, and $d_2 = 11.0\ \mu m$. The mode coupling characteristics, wavelength sensitivity, resolution, FOM, and other parameters are derived, and the results reveal maximum wavelength sensitivity of 49, 000 nm/RIU and average resolution of 3.64×10^{-6} RIU. With regard to commercial production, the minimum structural parameter sensitivity of the sensor is 50 nm/μm thus offering large tolerance in actual manufacturing. The sensor with outstanding properties and manufacturability has large potential in biomedicine, fiber optics, logging, geological exploration, and other applications.

Funding. City University of Hong Kong Donation Grant (9220061); City University of Hong Kong Strategic Research Grant (SRG 7005505); City University of Hong Kong Donation Research Grant (DON-RMG No. 9229021); Local Universities Reformation and Development Personnel Training Supporting Project from Central Authorities, Postdoctoral Scientific Research Development Fund of Heilongjiang Province (LBH-Q20081); Outstanding Young and Middle-Aged Research and Innovation Team of Northeast Petroleum University (KYCXTD201801); Natural Science Foundation of Heilongjiang Province (JQ2023F001).

Disclosures. The authors declare no conflicts of interest.

Data availability. Data underlying the results presented in this paper are not publicly available at this time but may be obtained from the authors upon reasonable request.

REFERENCES

1. T. G. Giallorenzi, J. A. Bucaro, A. Dandridge, G. H. Sigel, J. H. Cole, S. C. Rashleigh, and R. G. Priest, "Optical fiber sensor technology," IEEE Trans. Microw. Theory Tech. **30**, 472–511 (1982).
2. B. Lee, "Review of the present status of optical fiber sensors," Opt. Fiber Technol. **9**, 57–79 (2003).
3. P. Lu, N. Lalam, M. Badar, B. Liu, B. T. Chorpening, M. P. Buric, and P. R. Ohodnicki, "Distributed optical fiber sensing: Review and perspective," Appl. Phys. Rev. **6**, 041302 (2019).
4. Q. Li, J. Wang, H. Mu, J. Lv, L. Yang, Y. Shi, and C. Liu, "A Fabry–Pérot interferometer strain sensor composed of a rounded rectangular air cavity with a thin wall for high sensitivity and interference contrast," Opt. Commun. **527**, 128920 (2023).
5. A. D. Kersey, M. A. Davis, H. J. Patrick, M. LeBlanc, K. P. Koo, C. G. Askins, and E. J. Friebele, "Fiber grating sensors," J. Lightwave Technol. **15**, 1442–1463 (1997).
6. S. Roh, T. Chung, and B. Lee, "Overview of the characteristics of micro-and nano-structured surface plasmon resonance sensors," Sensors **11**, 1565–1588 (2011).
7. L. Xu, C. Liu, Y. Shi, Z. Yi, J. Lv, L. Yang, and P. K. Chu, "High-sensitivity photonic crystal fiber methane sensor with a ring core based on surface plasmon resonance and orbital angular momentum theory," Optik **286**, 170941 (2023).
8. L. Xu, C. Liu, H. Fu, J. Wang, X. Li, J. Lv, and P. K. Chu, "Orbital angular momentum-excited surface plasmon resonance for liquid refractive index sensing by photonic crystal fiber with high sensitivity and wide detection range," Opt. Eng. **61**, 096101 (2022).
9. L. B. Felsen, "Evanescent waves," J. Opt. Soc. Am. **66**, 751–760 (1976).
10. R. B. Zhong, W. H. Liu, J. Zhou, and S. G. Liu, "Surface plasmon wave propagation along single metal wire," Chin. Phys. B **21**, 117303 (2012).
11. L. B. Jeunhomme, *Single-Mode Fiber Optics: Principles and Applications* (Routledge, 2019).
12. E. Liu, S. Liang, and J. Liu, "Double-cladding structure dependence of guiding characteristics in six-fold symmetric photonic quasi-crystal fiber," Superlattices Microstruct. **130**, 61–67 (2019).
13. E. Liu, W. Tan, B. Yan, J. Xie, R. Ge, and J. Liu, "Robust transmission of orbital angular momentum mode based on a dual-cladding photonic quasi-crystal fiber," J. Phys. D **52**, 325110 (2019).
14. C. Li, B. Yan, and J. Liu, "Refractive index sensing characteristics in a D-shaped photonic quasi-crystal fiber sensor based on surface plasmon resonance," J. Opt. Soc. Am. A **36**, 1663–1668 (2019).
15. E. Liu and J. Liu, "Quasiperiodic photonic crystal fiber," Chin. Opt. Lett. **21**, 060603 (2023).
16. Y. Feng, W. Zhang, T. Xu, L. Huang, C. Liu, and T. Shen, "Design and research of a dual-parameter photonic crystal fiber sensor," J. Opt. Soc. Am. B **40**, 1267–1276 (2023).

17. N. Hussain, M. R. Masuk, M. F. Hossain, and A. Z. Kouzani, "Dual core photonic crystal fiber based plasmonic refractive index sensor with ultra-wide detection range," Opt. Express **31**, 26910–26922 (2023).
18. X. Liu, J. Yuan, Y. Qu, J. Zhang, X. Zhou, B. Yan, K. Wang, X. Sang, and C. Yu, "D-shaped photonic crystal fiber sensor based on the surface plasmon resonance effect for refractive index detection," Appl. Opt. **62**, E83–E91 (2023).
19. Q. Wang, X. Zhang, and X. Yan, "Design of a surface plasmon resonance temperature sensor with multi-wavebands based on conjoined-tubular anti-resonance fiber," Photonics **8**, 231 (2021).
20. Q. Chen, H. Chen, Y. Liu, Y. Wang, X. Fan, G. Bai, and H. Du, "A self-verification temperature sensor based on surface plasmon resonance in a hollow core negative curvature fiber," J. Phys. D **55**, 225208 (2022).
21. R. Slavík, J. Homola, and J. Čtyroký, "Single-mode optical fiber surface plasmon resonance sensor," Sens. Actuators B Chem. **54**, 74–79 (1999).
22. Q. M. Kamrunnahar, J. R. Mou, and M. Momtaj, "Dual-core gold coated photonic crystal fiber plasmonic sensor: Design and analysis," Results Phys. **18**, 103319 (2020).
23. J. Lv, H. Fu, C. Hu, Z. Yi, L. Yang, Y. Zeng, and C. Liu, "Double-formant surface plasmon resonance for refractive index sensing by anti-resonance fibers with high sensitivity and wide detection range," Results Phys. **40**, 105876 (2022).
24. I. S. Chronakis, "Micro-/nano-fibers by electrospinning technology: processing, properties and applications," Micromanuf. Eng. Technol. **2010**, 264–286 (2010).
25. J. Lin, J. B. Mueller, Q. Wang, G. Yuan, N. Antoniou, X. C. Yuan, and F. Capasso, "Polarization-controlled tunable directional coupling of surface plasmon polaritons," Science **340**, 331–334 (2013).
26. C. Liu, H. Fu, Y. Lv, Z. Yi, J. Lin, J. Lv, and P. K. Chu, "$HE_{1,1}$ mode-excited surface plasmon resonance for refractive index sensing by photonic crystal fibers with high sensitivity and long detection distance," Optik **265**, 169471 (2022).
27. W. Liu, Y. Shi, Z. Yi, C. Liu, F. M. Wang, X. L. Li, J. W. Lv, L. Yang, and P. K. Chu, "Surface plasmon resonance chemical sensor composed of a microstructured optical fiber for the detection of an ultra-wide refractive index range and gas-liquid pollutants," Opt. Express **29**, 40734–40747 (2021).
28. W. Liu, C. Liu, J. X. Wang, J. W. Lv, Y. Lv, L. Yang, N. An, Z. Yi, Q. Liu, C. J. Hu, and P. K. Chu, "Surface plasmon resonance sensor composed of microstructured optical fibers for monitoring of external and internal environments in biological and environmental sensing," Results Phys. **47**, 106365 (2023).
29. W. Liu, C. J. Hu, L. Zhou, Z. Yi, C. Liu, J. W. Lv, L. Yang, and P. K. Chu, "A square-lattice D-shaped photonic crystal fiber sensor based on SPR to detect analytes with large refractive indexes," Physica E **138**, 115106 (2022).
30. H. Fu, M. Zhu, C. Liu, Z. Yi, J. Lv, L. Yang, and P. K. Chu, "Photonic crystal fiber supporting 394 orbital angular momentum modes with flat dispersion, low nonlinear coefficient, and high mode quality," Opt. Eng. **61**, 026111 (2022).
31. Y. Xu, X. Chen, and Y. Zhu, "High sensitive temperature sensor using a liquid-core optical fiber with small refractive index difference between core and cladding materials," Sensors **8**, 1872–1878 (2008).
32. A. A. Revathi and D. Rajeswari, "Surface plasmon resonance biosensor-based dual-core photonic crystal fiber: design and analysis," J. Opt. **49**, 163–167 (2020).
33. F. Zha, J. Li, P. Sun, and H. Ma, "Highly sensitive selectively coated D-shape photonic crystal fibers for surface plasmon resonance sensing," Phys. Lett. A **383**, 1825–1830 (2019).
34. S. Revathi, S. R. Inabathini, and J. Pal, "Pressure and temperature sensor based on a dual core photonic quasi-crystal fiber," Optik **126**, 3395–3399 (2015).
35. M. B. Hossain, T. V. Mahendiran, L. F. Abdulrazak, I. M. Mehedi, M. A. Hossain, and M. M. Rana, "Numerical analysis of gold coating based quasi D-shape dual core PCF SPR sensor," Opt. Quantum Electron. **52**, 1–13 (2020).
36. S. Agarwal, J. H. Wendorff, and A. Greiner, "Use of electrospinning technique for biomedical applications," Polymer **49**, 5603–5621 (2008).
37. A. A. Rifat, M. R. Hasan, R. Ahmed, and H. Butt, "Photonic crystal fiber-based plasmonic biosensor with external sensing approach," J. Nanophotonics **12**, 012503 (2018).
38. M. R. Momota and M. R. Hasan, "Hollow-core silver coated photonic crystal fiber plasmonic sensor," Opt. Mater. **76**, 287–294 (2018).
39. E. Liu, B. Yan, H. Zhou, Y. Liu, G. Liu, and J. Liu, "OAM mode-excited surface plasmon resonance for refractive index sensing based on a photonic quasi-crystal fiber," J. Opt. Soc. Am. B **38**, F16–F22 (2021).
40. A. K. Mishra, S. K. Mishra, and B. D. Gupta, "SPR based fiber optic sensor for refractive index sensing with enhanced detection accuracy and figure of merit in visible region," Opt. Commun. **344**, 86–91 (2015).
41. F. Haider, R. A. Aoni, R. Ahmed, and A. E. Miroshnichenko, "Highly amplitude-sensitive photonic-crystal-fiber-based plasmonic sensor," J. Opt. Soc. Am. B **35**, 2816–2821 (2018).
42. M. S. Islam, C. M. Cordeiro, J. Sultana, R. A. Aoni, S. Feng, R. Ahmed, and D. Abbott, "A Hi-Bi ultra-sensitive surface plasmon resonance fiber sensor," IEEE Access **7**, 79085–79094 (2019).
43. V. Kaur and S. Singh, "Design of titanium nitride coated PCF-SPR sensor for liquid sensing applications," Opt. Fiber Technol. **48**, 159–164 (2019).